Research Square

Preprints are preliminary reports that have not undergone peer review.
They should not be considered conclusive, used to inform clinical practice,
or referenced by the media as validated information.

Vertically Partitioned Interfacial Design in Self-Powered Perovskite Photomemristors Enables CMOS-Integrated Motion Vision System

Ding Zheng

dingzheng@uestc.edu.cn

University of Electronic Science and Technology of China https://orcid.org/0000-0002-6420-733X

Lunyao Pan

Southwest Jiaotong University

Shixiu Sun

University of Electronic Science and Technology of China

Xu Zhang

University of Electronic Science and Technology of China

Lin Gao

University of Electronic Science and Technology of China

Yujie Peng

University of Electronic Science and Technology of China

Jianghao Tian

University of Electronic Science and Technology of China

Zirui Tian

University of Electronic Science and Technology of China

Zhennan Tian

University of Electronic Science and Technology of China

Haozhe Liu

University of Electronic Science and Technology of China

Haihong Guo

University of Electronic Science and Technology of China

Qiao Luo

University of Electronic Science and Technology of China

Taiyu Li

University of Electronic Science and Technology of China

Junsheng Yu

University of Electronic Science and Technology of China https://orcid.org/0000-0002-7484-8114

Article

Keywords:

Posted Date: June 22nd, 2026

DOI: https://doi.org/10.21203/rs.3.rs-10075143/v1

License: This work is licensed under a Creative Commons Attribution 4.0 International License.
Read Full License

Additional Declarations: There is **NO** Competing Interest.

Abstract

Photomemristive artificial synapses, which integrate optical sensing, memorizing, and preprocessing, offer a new route for neuromorphic vision systems that avoid high computational power demands. However, for most perovskite photomemristors devices with a simple metal-semiconductor junctions, the interfacial origin of persistent optical memory remains poorly understood, which has limited the optimal design of device architecture. In this work, we report a vertically partitioned interfacial architecture for self-powered metal-halide perovskite photomemristors. For the buried interface, P3HT directs perovskite crystallization and establishes a hole selective photovoltaic pathway, whereas the polymer overlayer conventionally used for encapsulation or passivation is redefined as an active ion-electron relaxation interphase. To modify the top interface of the perovskite layer, a series of insulating polymers with different terminal groups were screened. Among them, PBMA was identified as the optimal top interphase, which is attributed to the fact that Pb coordinating ester carbonyls stabilize iodide redistribution, while the butyl side chain environment prolongs electron side recovery. This vertically partitioned architecture stabilizes photoinduced conductance states without external bias, yielding a 119% paired pulse facilitation index and the most persistent cumulative conductance modulation among the polymer series. Furthermore, when integrated with a 640 · 512 CMOS readout platform with 15 μm pixels, the optimized stack enables hardware level motion direction recognition and trajectory recording, increasing the downstream clustering score from 0.6011 to 0.9090. This work establishes a vertically partitioned interfacial architecture as a structural basis for self-powered perovskite photomemristors and interface-defined neuromorphic vision hardware.

Introduction

The rapid expansion of artificial intelligence (AI) workloads has exposed the limitations of conventional von Neumann architectures, in which repeated data shuttling between physically separated sensors, memories and processors leads to substantial latency and energy overhead[1, 2, 3]. Memristive devices, whose conductance can be continuously modulated and retained by the history of external stimuli, offer a compact route to integrate sensing, storage and computation within the same hardware unit. This requirement is particularly acute in visual perception, where dynamic scenes generate massive redundant spatiotemporal data before feature extraction, driving the need for devices that detect, store and preprocess optical signals at the sensing terminal for neuromorphic vision[4, 5, 6, 7]. Photomemristors address this requirement by coupling photodetection with history-dependent conductance modulation, allowing optical variables such as wavelength, intensity, duration and pulse frequency to be stored as persistent conductance states rather than only being converted into transient photocurrents[8, 9, 10]. Conventional optoelectronic memristive vision systems have often relied on circuit-level integration, in which photodiodes or phototransistors first convert optical inputs into electrical signals that are subsequently stored or processed by separate memristive elements. Although one-photodiode-one-memristor crossbars and multi-phototransistor-one-memristor arrays have enabled in-sensor visual memorization, optical encoding and reconfigurable image processing, the spatial separation between

phototransduction and memory increases device count, interconnect density and system-level overhead[11, 12, 13]. This has motivated intrinsically photomemristive materials in which light absorption, carrier generation and conductance evolution occur within the same active element[14, 15]. Representative platforms include electro-iono-photoactive two-dimensional neuristors[16], monolayer transition-metal dichalcogenide memitters[17], oxide-based photomemristors and organic optoelectronic memristors[18, 19]. These systems have advanced neuromorphic vision from circuit assembly toward intrinsic device functionality, but they do not yet fully resolve how photogeneration, carrier separation and post-illumination relaxation should be coordinated within a single scalable device[20, 21].

Metal halide perovskites provide a particularly attractive material basis for intrinsic photomemristors because strong optical absorption, long carrier diffusion lengths, defect-tolerant semiconducting behaviour and mixed ionic-electronic transport coexist in a soft ionic lattice[22, 23, 24]. In such materials, photogenerated carriers respond on electronic time scales, whereas halide ions and vacancies redistribute more slowly under optical or electrical excitation[25, 26]. The resulting ion-electron coupling can modulate interfacial barriers, local doping, band bending and carrier lifetime, enabling optical synaptic behaviours such as paired-pulse facilitation, conductance retention and memory consolidation. Perovskite photomemristors have therefore progressed from two-dimensional perovskite light-modulated plasticity[27, 28] and monolithic perovskite photonic synapses[29] to non-volatile memory transistors[30] and retinomorphic imaging arrays[31]. Photomemristive devices differ from perovskite photovoltaics and light-emitting diodes, where charge-selective layers and interfacial modifiers are usually introduced within an already established operational architecture[32, 33]. In many two-terminal perovskite synaptic devices, the active perovskite is still placed between two electrodes in a simplified metal-insulator-metal-type geometry. Although such structures can produce light or field-history-dependent conductance modulation, they do not explicitly define where photovoltaic carrier separation, mobile-ion redistribution and electronic recovery should occur. For self-powered photomemristors, interface engineering must therefore become architecture engineering: the device requires a buried interface that establishes built-in carrier separation and a top recovery interface that programs ion-electron relaxation.

Here we report a vertically partitioned architecture strategy for self-powered $MAPbI_3$ photomemristors, in which a simple electrode/perovskite/electrode stack is reorganized into a functionally defined photomemristive structure. The P3HT/$MAPbI_3$ buried interface directs $MAPbI_3$ crystallization and provides a hole-selective, built-in carrier-separation pathway, whereas the $MAPbI_3$/polymer top interface is redefined from a conventional passivation or encapsulation layer into a chemically programmable ion-electron recovery interphase. By screening polymer interfaces bearing hydroxyl, phenyl, lactam-carbonyl, ester-carbonyl and butyl-substituted ester-carbonyl motifs, we identify PBMA as the optimal top interphase. Ester-carbonyl/Pb coordination stabilizes the Pb-I framework and restricts iodide redistribution toward the top interface, while the butyl side-chain environment prolongs electron-side relaxation. This spatial assignment of carrier separation and ion-electron recovery stabilizes

photoinduced conductance states under zero-bias operation and enables self-powered optical synaptic plasticity. The optimized stack is further integrated with a 640 × 512 CMOS readout platform with 15 μm pixels, enabling hardware-level motion-direction recognition and trajectory recording, with downstream clustering scores increasing from 0.6011 to 0.9090 after 10 optical pulses. This work establishes a vertically partitioned interfacial architecture as a structural foundation for self-powered perovskite photomemristors, in which crystallization-directed carrier separation and chemically programmed ion-electron recovery are assigned to distinct interfaces to guide future optoelectronic memristive device design.

Results

Buried-interface regulation of $MAPbI_3$ crystallization

The buried interface was engineered as the lower functional boundary of the vertically partitioned photomemristive architecture. In a self-powered photomemristor, this interface must simultaneously guide $MAPbI_3$ crystallization and establish the built-in asymmetry required for carrier separation. P3HT was therefore introduced beneath $MAPbI_3$ as a crystallization-directing and hole-selective buried contact, followed by brief ultraviolet-ozone treatment to improve precursor wetting (Fig. 1a). This construction assigns crystallization-directed carrier separation to the buried interface, while reserving ion-electron recovery for the $MAPbI_3$/polymer top interface. In Fig. 1b, Photoluminescence (PL) provides the optical signature of buried-interface regulation. Compared with $MAPbI_3$ grown directly on the substrate, the P3HT-assisted film exhibits enhanced PL intensity and a blue-shifted emission maximum from 771 to 767 nm, suggesting suppressed trap-assisted non-radiative recombination and a reduced contribution from lower-energy defect-tail emission[34]. These changes are consistent with reduced shallow interfacial traps associated with undercoordinated Pb/I-related sites and a more ordered local crystallization environment at the P3HT/$MAPbI_3$ buried interface. To directly probe this buried interface, a peel-off strategy was used to remove the $MAPbI_3$ overlayer and expose the P3HT/$MAPbI_3$ interface for further analysis (Fig. 1c). The peel-off FTIR spectra provide molecular-level evidence that the P3HT/$MAPbI_3$ buried interface is not a purely mechanical contact. After $MAPbI_3$ removal, the C = C stretching vibration of the exposed P3HT layer shifts from 1511 to 1516 cm^{-1}, while the main backbone-related features remain discernible (Fig. 1d)[35]. Because this spectral shift is retained after physical separation of the $MAPbI_3$ overlayer, it indicates that the local electronic environment of the P3HT backbone has been perturbed during $MAPbI_3$ growth, consistent with interfacial interaction between Lewis-basic thiophene S atoms and undercoordinated Pb sites. The $MAPbI_3$-side FTIR spectra further show changes in N-H, C-N and C-H related vibrations (Fig. 1e), indicating that the methylammonium coordination and hydrogen-bonding environment are also altered by the P3HT buried interface[36]. These two-sided vibrational responses support a chemically coupled buried interface that regulates perovskite nucleation and PbI_6 octahedral assembly, rather than a mechanically stacked P3HT/$MAPbI_3$ bilayer[37].

The interfacial templating effect is further corroborated by the crystallographic and morphological characterizations. The grazing-incidence wide-angle X-ray scattering (GIWAXS) patterns and the corresponding azimuthally integrated profiles (Fig. 1f-h) reveal that $MAPbI_3$ grown on P3HT adopts a crystallographic organization distinct from that of the control film grown directly on the substrate. Scanning electron microscopy (SEM) and X-ray diffraction (XRD) analyses further support this buried-interface templating effect: $MAPbI_3$ forms a more continuous morphology on treated P3HT, while the reduced PbI_2/$MAPbI_3$ (110) intensity ratio indicates suppressed residual intermediate phase PbI_2 formation and improved perovskite crystallization (**Supplementary Figs. 1 and 2**)[38]. In summary, the P3HT buried interface suppresses interfacial defect recombination and promotes $MAPbI_3$ crystallization. Together with the established hole-transporting nature of P3HT, this buried contact provides a hole-selective pathway for self-powered carrier separation.

Side-chain-defined MAPbI/polymer top interface

During post photoexcitation relaxation in $MAPbI_3$, iodide migration and photogenerated electron transport are coupled at the top interface. In perovskite optoelectronics, polymer overlayers are commonly introduced for encapsulation, environmental stabilization, or defect passivation[39]. Here, the $MAPbI_3$/polymer contact is instead developed as a chemically defined interphase for regulating top-interface ion-electron coupling, where Pb-site coordination, Pb-I framework stabilization, iodide redistribution and electron-side relaxation are coupled within the same interface. Previous studies have established that side-chain-defined interfacial chemical environments strongly influence interfacial electronic relaxation[40]. We therefore focus on side-chain differentiation under a comparable polymer-backbone framework. The chemically differentiated polymer series comprises PVA, PS, PVP, PMMA and PBMA, exposing hydroxyl, phenyl, lactam carbonyl, ester carbonyl and butyl-substituted ester carbonyl motifs, respectively (Fig. 2a and **Supplementary Fig. 3**). This polymer series was selected to decouple two molecular factors that are expected to determine top-interface relaxation: the availability of Lewis-basic coordination sites and the steric/electrostatic environment surrounding these sites. PVA provides hydroxyl groups that can interact with polar surface species but do not offer a strongly oriented carbonyl donor for Pb-site anchoring. PS contains a non-polar phenyl side group and therefore mainly probes weak van der Waals-type contact with limited coordination capability. PVP introduces a lactam carbonyl embedded in a cyclic side group, providing a stronger Lewis-basic motif but with different orientation and steric accessibility from methacrylate esters. PMMA and PBMA both contain ester carbonyls that can coordinate undercoordinated Pb sites, but PBMA further introduces a longer butyl side chain that modifies the local dielectric, hydrophobic and steric environment around the coordination site. This comparison therefore provides a molecular screening framework: an effective top interphase should combine accessible Pb-coordinating groups, sufficient interfacial charge transfer, a raised iodide-migration barrier and a side-chain environment that prolongs electronic relaxation without blocking electron transport[41].

Electrostatic-potential mapping further reveals how side-chain chemistry reshapes the local electrostatic environment at the $MAPbI_3$/polymer top interface. PBMA exhibits a more positive electrostatic-potential distribution around the butyl-substituted side-chain region, indicating that the longer alkyl side chain reshapes the local electrostatic environment relevant to electron-side relaxation (Fig. 2b, d). The calculated binding energies quantify the interaction between the polymer motifs and the $MAPbI_3$ top surface (Fig. 2c, e). The optimized adsorption geometries provide the structural basis for this comparison, showing how each side-chain motif approaches the $MAPbI_3$ surface before energy and migration-barrier analysis (**Supplementary Fig. 4**). PBMA exhibits the strongest binding energy of -0.83 eV, indicating the most stable contact with Pb-related defect sites. This stronger interaction stabilizes the perovskite lattice framework and suppresses defect configurations that favor iodide migration[42, 43]. The I^- migration-energy profiles reveal that ester-carbonyl interfaces raise the kinetic barrier for iodide displacement, with PBMA producing the least favorable migration pathway among the polymer series (Fig. 2f and **Supplementary Fig. 5**). Differential charge-density maps and transferred-electron profiles show that PBMA-modified $MAPbI_3$ exhibits the strongest interfacial charge transfer, indicating favorable electronic coupling at the $MAPbI_3$/PBMA top interface (Fig. 2g). Taken together, the DFT results establish that binding strength alone is not the only selection criterion for the top interphase. The optimal polymer should simultaneously stabilize Pb-related surface sites, increase the barrier for iodide displacement, preserve interfacial charge transfer and create a side-chain environment that moderates electron-side recovery. PBMA satisfies these requirements most effectively: the ester carbonyl coordinates with undercoordinated Pb sites and stabilizes the local Pb-I octahedral framework, whereas the butyl side chain introduces steric confinement that prolongs electron-side relaxation. This combined ionic and electronic regulation provides the molecular basis for persistent self-powered optical memory (Fig. 2h).

Top-interface ion-electron relaxation mechanism

The chemical, ionic and electrical signatures of the $MAPbI_3$/polymer top interface were examined to clarify how molecular design regulates ion-electron relaxation. Pb 4f XPS spectra show polymer-dependent changes in the Pb-related chemical environment, indicating that the top polymers interact with Pb-related surface sites rather than forming electronically inert overlayers (Fig. 3a). After PBMA modification, the Pb 4f signal shifts relative to pristine $MAPbI_3$, consistent with electron-density redistribution around Pb-related surface sites and coordination between Lewis-basic ester carbonyl groups and undercoordinated Pb defects. The FTIR spectra of pristine PBMA and PBMA deposited on $MAPbI_3$ further show a shift of the carbonyl-related vibration after interfacial contact, confirming that the ester carbonyl participates in binding at the $MAPbI_3$/PBMA interface rather than remaining chemically inactive (Fig. 3b). The O 1s and I 3d XPS spectra, together with the $MAPbI_3$/polymer FTIR spectra, further establish a side-chain-dependent chemical response across the polymer series (**Supplementary Figs. 6–8**). Transient absorption measurements extend this chemical picture to carrier dynamics, showing that

polymer modification alters photocarrier relaxation rather than acting as an optically inert encapsulation layer (**Supplementary Fig. 13**).

Light-excited ToF-SIMS depth profiling was then used to track ionic redistribution under the 375 nm optical-excitation configuration (Fig. 3c and **Supplementary Figs. 9–12**). PBMA gives the weakest iodine enrichment in the polymer and near-surface regions, whereas PbI_2-related signals vary only slightly among the polymer-modified systems. These depth-resolved ion profiles indicate that the polymer-dependent relaxation is governed mainly by iodide redistribution rather than Pb-related migration. The suppressed iodine accumulation at the $MAPbI_3$/PBMA interface supports the role of ester-carbonyl/Pb coordination in stabilizing the Pb-I framework and restricting photoinduced iodide migration toward the top interface during post-excitation recovery. By reducing iodine accumulation, PBMA mitigates ion-assisted electrostatic compensation of accumulated photoelectrons, thereby suppressing excessive interfacial self-n-doping and band bending while preserving electron transport across the top interface[45]. Electrical and electrostatic measurements further connect this restrained ionic redistribution with device-level recovery dynamics. In complete ITO/P3HT/$MAPbI_3$/polymer/Ag devices, voltage-dependent impedance spectra reflect the combined contributions of electronic transport, interfacial polarization, trap charging and ion-mediated relaxation (Fig. 3d). Compared with hydroxyl-, phenyl- and lactam-carbonyl-based interfaces, PMMA and PBMA show more stable interfacial charge accumulation and relaxation, with PBMA exhibiting the most stable transition behaviour and a higher-voltage low-frequency transition. Capacitance-voltage characteristics provide complementary evidence that ester-carbonyl-containing interfaces support more favourable charge accumulation, while the PBMA side-chain environment slows rapid ion-coupled polarization and prolongs electron-side recovery (Fig. 3e). Frequency-dependent impedance maps further separate fast electronic transport from slower interfacial polarization and ion-related relaxation (**Supplementary Fig. 14**). KPFM, depth-resolved UPS and the derived band diagrams reveal moderated electrostatic and energetic perturbation at the $MAPbI_3$/PBMA interface, consistent with restrained iodide redistribution and controlled electron recovery (Fig. 3f and **Supplementary Figs. 15–19**)[48, 49]. Optical-field and drift-diffusion simulations support this assignment. FDTD simulations show that polymer insertion redistributes the local optical field across the $MAPbI_3$/polymer/Ag top interface, while Poisson-drift-diffusion simulations indicate that PBMA maintains a moderate electron-rich interfacial state without the excessive charge localization observed for PS (**Supplementary Figs. 20 and 21** and **Supplementary Note 1**). These results identify PBMA as a balanced ion-electron relaxation interphase rather than a layer that simply blocks ions or maximizes charge accumulation.

Together, these chemical, ionic, electrical and energetic signatures establish a mechanistic link between top-interface molecular design and persistent self-powered optical memory. The P3HT/$MAPbI_3$ buried contact provides crystallization-directed and hole-selective carrier separation, whereas the $MAPbI_3$/PBMA top interphase programs post-excitation recovery through ester-carbonyl/Pb-stabilized iodide redistribution and butyl-side-chain-prolonged electron relaxation (Fig. 3g). Complete-device controls further verify the structural necessity of this vertically partitioned interfacial architecture:

ITO/$MAPbI_3$/Ag shows negligible cumulative modulation, while ITO/P3HT/$MAPbI_3$/Ag shows only weak pulse-dependent memory under 200 consecutive 375 nm optical pulses (**Supplementary Fig. 22**). After introducing polymer top interphases, ester-carbonyl-containing PMMA and PBMA devices exhibit stronger cumulative photoresponses, with PBMA showing the most persistent modulation. Paired-pulse measurements further quantify this residual interfacial memory, with PBMA reaching the highest PPF index of 119%, exceeding PMMA (101%), PVP (97%), control (91%), PVA (89%) and PS (88%) (**Supplementary Fig. 23a, b**). These device-level results demonstrate that the optimized photomemristive response arises from structural cooperation between a carrier-separating buried interface and an ion-electron recovery top interface, rather than from simple polymer modification.

Self-powered optical synaptic plasticity

After the comparative device-level analysis identified PBMA as the top interface with the strongest facilitation response, we next examined the synaptic characteristics of the optimized ITO/P3HT/$MAPbI_3$/PBMA/Ag device. Figure 4a illustrates the device-to-synapse analogy: optical excitation generates a self-powered postsynaptic current, while incomplete interfacial recovery stores optical history as a conductance state. PPF provides direct evidence for short-term optical memory under self-powered operation. Under both 520 and 375 nm optical excitation, the PPF index decreases with increasing interpulse interval (Fig. 4b**)**, indicating that facilitation occurs only when the second pulse arrives before complete recovery of the $MAPbI_3$/PBMA top interphase. This interval-dependent response arises from residual electron accumulation and ion-coupled polarization that retard recovery of the interfacial electric-field state. The photosynaptic current further scales with optical dose. At a fixed pulse duration of 1.5 s, increasing the optical power density enhances the current response (Fig. 4c), whereas at a fixed power density, extending the pulse duration strengthens conductance modulation (Fig. 4d). These results show that the optimized device encodes both intensity and temporal information under zero-bias operation. Pulse-train measurements further distinguish this response from a simple photoconductive transient. When the number of 300 ms optical excitation pulses is increased, the synaptic current accumulates progressively (Fig. 4e), reflecting stepwise occupation of a metastable interfacial relaxation state governed by the $MAPbI_3$/PBMA top interphase. The learning-forgetting-relearning process in Fig. 4f shows that a previous 15-pulse training sequence leaves a residual conductance state, enabling faster relearning after a 5 s interval. The responses to 1, 5, 10 and 50 pulses in Fig. 4g further reveal a transition from short-term memory to long-term memory, consistent with gradual consolidation of the photoinduced interfacial state.

These synaptic characteristics clarify the interfacial requirements for high-performance optoelectronic memristive synapses. Unlike photovoltaic or light-emitting perovskite devices, where slow ionic relaxation and interfacial hysteresis are generally minimized, a photomemristors requires a controlled recovery pathway that preserves part of the photo-induced interfacial state after excitation. The interface should suppress uncontrolled iodide accumulation, maintain interfacial electron transport and prolong electron-side relaxation. In the present vertically partitioned interfacial architecture, the P3HT/$MAPbI_3$

buried contact provides self-powered carrier separation, whereas the $MAPbI_3$/PBMA top interphase regulates ion-electron recovery through ester-carbonyl/Pb-stabilized iodide redistribution and butyl-side-chain-mediated electronic relaxation. The PPF decay, pulse-number-dependent accumulation, learning-forgetting-relearning behaviour and short-to-long-term memory transition therefore arise from a chemically programmed recovery interface, rather than from simple photoconductive gain or unstable filamentary switching. The PBMA concentration series and storage test further confirm the processing window and stability of this top recovery interphase (**Supplementary Figs. 24 and 25**). To examine whether the vertically partitioned interfacial architecture is limited to single-cation $MAPbI_3$, the same P3HT buried interface and PBMA top interphase were implemented in mixed-cation $Cs_{0.05}FA_{0.95}PbI_3$, which retains pulse-dependent conductance modulation, delayed recovery and learning-forgetting-relearning behaviour (**Supplementary Fig. 26**). These device-level measurements show that the optimized photomemristive response arises from the vertically partitioned interfacial architecture, in which the buried interface establishes carrier separation and the top relaxation interphase programs ion-electron relaxation, rather than from simple polymer modification.

CMOS-integrated hardware-level motion-state recognition and algorithmic trajectory clustering

The self-powered interfacial photomemristors was further implemented in a CMOS-integrated perovskite visual array. In this platform, the optimized P3HT/$MAPbI_3$/PBMA photomemristive stack forms a 640 × 512-pixel array with a pixel size of 15 μm and functions as the light-sensitive memory layer directly coupled to the readout integrated circuit (ROIC) (Fig. 5a-c). The imaging platform was constructed by integrating the perovskite/ROIC module into a camera unit, allowing projected optical patterns to be acquired and retained by the photomemristive pixels before circuit-level readout (Fig. 5b and **Supplementary Fig. 27**). Unlike conventional CMOS sensors that mainly record instantaneous photocurrent, the CMOS-integrated perovskite array preserves the relaxation dynamics of the self-powered photomemristor during imaging. The time-resolved images in Fig. 5d demonstrate hardware-level recognition of six motion states at t_1 = 0 s, t_2 = 1.5 s and t_3 = 3 s. For each motion direction, residual signals from previous positions coexist with newly illuminated regions, converting sequential optical inputs into fading trajectory maps. Dynamic imaging of the university emblem verifies hardware-level trajectory retention for patterned visual inputs, with frames extracted at t_1 = 0 s, t_2 = 1 s, t_3 = 2 s, t_4 = 3 s and t_5 = 4 s reconstructing the emblem motion (**Supplementary Fig. 28**). This trajectory retention originates from the same stabilized relaxation pathway that underlies the single-device synaptic response. Therefore, the perovskite array performs front-end motion-trajectory recording of dynamic optical inputs before algorithmic analysis.

The wavelength-dependent gain asymmetry further supports hardware-level preprocessing of dynamic visual inputs. At an integration time of 0.5 s, the paired-pulse facilitation factors are 106.988% under 520 nm illumination and 130.7% under 375 nm illumination. In this demonstration, the weaker 520 nm

response was encoded as the background channel, whereas the stronger 375 nm response was encoded as the target-signal channel. Under repeated optical stimulation, this differential gain physically enhances the target-related motion response before digital analysis, producing hardware-encoded motion streams with improved foreground-background contrast (**Supplementary Figs. 29 and 30**, **Supplementary Note 2**). The brightness-distribution statistics further show that device-level preprocessing concentrates the initially broad pixel-intensity distribution into a more target-dominant high-brightness regime (**Supplementary Fig. 31**). These results show that the CMOS-integrated perovskite photomemristor array performs front-end motion-state encoding and spatiotemporal memory before algorithmic processing. The hardware-encoded trajectory maps were subsequently used as inputs for algorithmic evaluation. The algorithmic workflow is detailed in **Supplementary Note 3**, where the hardware-encoded trajectory maps were normalized, embedded into a two-dimensional feature space and clustered using a density-based unsupervised approach. Unsupervised clustering was applied to six-direction motion data obtained from the ideal noiseless state, the initial pulse-1 state and the enhanced pulse-10 state (Fig. 5e-g). The ideal noiseless state gives a clustering score of 0.9128, defining the reference separability for the six motion categories (Fig. 5e). The initial pulse-1 state yields a lower score of 0.6011, indicating insufficient accumulation of interfacial memory and weakly separated direction features (Fig. 5f). After ten optical pulses, the enhanced state reaches a clustering score of 0.9090, approaching the ideal reference and demonstrating that hardware-level optical memory improves the separability of motion features before software classification (Fig. 5g). Consistently, device-level preprocessing increases the silhouette coefficient from 0.5961 to 0.9131. The same hardware-to-algorithm workflow is further extended to digit- and shoes-recognition tasks, where device-level gain modulation improves the input representation before downstream inference (**Supplementary Figs. 32 and 33**, **Supplementary Notes 4** and **5**). These results indicate that the vertically partitioned photomemristive stack transfers single-device interfacial relaxation dynamics to array-level motion recording, while downstream clustering evaluates the separability of the device-generated motion features.

Conclusion

This work establishes a vertically partitioned interfacial architecture for self-powered $MAPbI_3$ photomemristors. Rather than treating the perovskite stack as a single mixed ionic-electronic medium, we assign crystallization control, built-in carrier separation and ion-electron recovery to two complementary interfaces. The P3HT/$MAPbI_3$ buried interface as a crystallization-directing and hole-selective carrier-separation contact, whereas the $MAPbI_3$/PBMA top interface transforms a conventional polymer overlayer into a chemically programmable recovery interphase. By coordinating buried-interface growth control with top-interface ion-electron recovery, optical inputs are retained as history-dependent conductance states under zero-bias operation. Extension to mixed-cation $Cs_{0.05}FA_{0.95}PbI_3$ further indicates that this interfacial architecture is not restricted to $MAPbI_3$, but can operate across iodide perovskites with different A-site compositions. The CMOS-integrated 640 × 512 array verifies that this architecture can be translated into hardware-level motion-direction recognition and trajectory recording,

followed by downstream evaluation of device-generated motion features. More broadly, this work defines a molecular selection rule for top recovery interphases: accessible Pb-coordinating motifs and a suitable side-chain environment should stabilize iodide redistribution, preserve interfacial electron transport and prolong electronic relaxation. Overall, the vertically partitioned interfacial architecture provides a structural basis for coordinating perovskite crystallization, built-in carrier separation and ion-electron recovery in future self-powered optoelectronic memristive devices.

Methods

Materials

Poly(3-hexylthiophene-2,5-diyl) (P3HT), lead(II) iodide (PbI_2, 99.99%), methylammonium iodide (MAI, 99.99%), formamidinium iodide (FAI, 99.9%), cesium iodide (CsI, 99.999%), N,N-dimethylformamide (DMF, 98%), dimethyl sulfoxide (DMSO, 98%), chlorobenzene (CB, 99%), poly(vinyl alcohol) (PVA, 99%), polystyrene (PS, 99%), poly(vinylpyrrolidone) (PVP, 99%), poly(methyl methacrylate) (PMMA, 99%), and poly(butyl methacrylate) (PBMA, 99%) were obtained from Shanghai Macklin Co, Ltd. The ROIC used for array-level imaging was the IR640 readout integrated circuit (ROIC), which contains a 640 × 512-pixel array with a pixel size of 15 μm. The ROIC employs stripe-like Au common electrodes and spatially isolated patterned Au bottom electrodes at the pixel level; the top electrode is required to provide continuous interconnection between the pixel area and the common-electrode pad while remaining optically transmissive. The chip operates at 1.8 V for analog/digital supply and 3.3 V for I/O, with a typical power consumption of 60 mW, adjustable integration time from 50 μs to 15 ms in 10 μs steps, a typical read noise of 230 e^-, a full-well capacity of 460 ke^-, a 50-fps frame rate, a 5 MHz system clock, and four differential analog output channels.

Fabrication of perovskite heterostructures and photomemristive devices

Indium tin oxide (ITO)-coated glass substrates with a 120 nm ITO layer were sequentially cleaned with deionized water, acetone and isopropyl alcohol, dried under nitrogen and treated with ultraviolet-ozone for 10 min. P3HT in chlorobenzene (5 mg mL^{-1}) was spin-coated onto ITO at 3000 rpm for 5 min and annealed at 100°C for 10 min, followed by low-power ultraviolet-ozone treatment for 10 min. $MAPbI_3$ precursor solution was prepared by dissolving methylammonium iodide and PbI_2 at a molar ratio of 1:1 in DMF/DMSO mixed solvent (4:1, v/v) with a total concentration of 1.2 M. The solution was stirred at 60°C for 12 h and filtered through a 0.22 μm polytetrafluoroethylene (PTFE) filter before use. $MAPbI_3$ films were deposited by a one-step antisolvent method at 1000 rpm for 10 s and 4000 rpm for 30 s, during which 150 μL chlorobenzene was dropped 20 s after the start of the second step, followed by annealing at 100°C for 10 min. For the mixed-cation $Cs_{0.05}FA_{0.95}PbI_3$ devices, PbI_2 (912 mg) and FAI (294 mg) were dissolved in a DMF/DMSO mixed solvent (9:1, v/v), followed by the addition of 64.3 μL CsI/DMSO solution (363.73 mg mL^{-1}). The resulting precursor was used to deposit $Cs_{0.05}FA_{0.95}PbI_3$ films

using the same spin-coating and annealing procedures. PVA, PS, PVP, PMMA and PBMA were separately dissolved in chlorobenzene at 5 mg mL^{-1}, spin-coated onto $MAPbI_3$ at 4000 rpm for 5 min and annealed at 100°C for 3 min. For concentration-dependent studies, only the PBMA concentration was varied. Finally, 100 nm Ag was deposited by vacuum vapor deposition to form ITO/P3HT/$MAPbI_3$/polymer/Ag devices, where polymer denotes PVA, PS, PVP, PMMA or PBMA. All perovskite-related preparation processes were carried out in a nitrogen-filled glovebox.

Integration of the perovskite device with the ROIC chip

For imaging-array integration, the perovskite heterostructure was fabricated directly on the IR640 ROIC using the supplier-recommended masking and interconnection process. The chip was first transferred onto a glass carrier and fixed with low-adhesion double-sided tape under microscope assistance. High-temperature tape was then applied to protect the bonding pads and common-electrode region while leaving the pixel area exposed, after which the P3HT, $MAPbI_3$ and polymer layers were sequentially deposited to uniformly cover the pixel array. Following removal of the tape over the common electrode, a continuous and optically transmissive top electrode was formed to electrically interconnect the pixel region and the common-electrode pad, thereby establishing the vertical transport path required for ROIC readout. The IR640 readout integrated circuit (ROIC) contains a 640 × 512-pixel array with a pixel size of 15 μm, employs stripe-like Au common electrodes and isolated Au pixel electrodes, and is intended for top-illumination vertical detectors in which the readout circuit collects holes. The integrated perovskite/ROIC imager was operated in the integrate-while-read (IWR) mode and read out through four differential analog output channels. Throughout fabrication, the tape edges were kept tightly attached, the common-electrode region was masked last, the pad region was kept clean, and highly adhesive tapes, sharp tools and direct contact with the pixel area were avoided to prevent chip damage. For the visual-imaging experiments, the assembled perovskite/ROIC chip was coupled to the external imaging platform shown in Supplementary Fig. 27 and operated under the optical conditions described in the main text.

Characterizations

The crystalline structure of $MAPbI_3$ films was investigated by X-ray diffraction (XRD; X'Pert Pro X-ray diffractometer) using Cu Kα radiation (λ = 1.5418 Å). The surface morphology of the films was characterized using a scanning electron microscope (SEM; JEOL JSM-7800 Prime) operated at an accelerating voltage of 5 kV. Grazing-incidence wide-angle X-ray scattering (GIWAXS) measurements were performed at the BL14B1 beamline of the Shanghai Synchrotron Radiation Facility. UV-vis absorption spectra were recorded using a UV-2500 spectrophotometer (Shimadzu Corporation). Steady-state photoluminescence (PL) spectra were measured using an FLS980 spectrometer (Edinburgh Instruments) equipped with a 450 W xenon lamp. Fourier-transform infrared (FTIR) spectra were obtained using a TENSOR II spectrometer (Bruker) with a spectral resolution of 4 cm^{-1}. X-ray photoelectron spectroscopy (XPS) measurements were performed using a Thermon Fisher Scientific K-Alpha+ spectrometer with a monochromatic Al Kα X-ray source, and the binding energies were calibrated with reference to the C 1s peak at 284.8 eV. Time-of-flight secondary-ion mass spectrometry (ToF-SIMS)

depth profiles were collected using an ION-TOF TOF.SIMS 5 instrument. For light-induced ion-redistribution measurements, the samples were measured under the 375 nm optical-excitation configuration shown in Supplementary Fig. 9. Transient absorption spectra were recorded using a Helios Fire transient absorption spectrometer (Ultrafast Systems) to compare carrier dynamics in pristine and polymer-modified $MAPbI_3$ films. Kelvin probe force microscopy (KPFM) measurements were performed using a Bruker Dimension Icon atomic force microscope. Ultraviolet photoelectron spectroscopy (UPS) was performed using a Thermo Scientific ESCALAB 250Xi system to analyse the depth-dependent energy-level evolution of polymer/$MAPbI_3$ interfaces. Electrical and optoelectronic measurements were performed on ITO/P3HT/$MAPbI_3$/polymer/Ag devices. Current-voltage characteristics and pulse-train photoresponses were recorded using a Keithley 4200A-SCS parameter analyser. Capacitance-voltage characteristics were measured using a Keithley 4200A-SCS parameter analyser. Impedance spectra were collected using a Zahner Zennium electrochemical workstation. Paired-pulse facilitation, optical-dose-dependent responses, learning-forgetting-relearning behaviour and memory-consolidation measurements were conducted under the conditions specified in the corresponding figure captions. CMOS-integrated imaging was performed using the perovskite/ROIC chip and the external imaging platform shown in Supplementary Fig. 27.

DFT calculations

The first-principle calculations were carried out within density-functional theory (DFT), implemented in the Vienna Ab Initio Simulation Package (VASP) code[51], using the frozen-core projector augmented-wave (PAW) method to describe the interaction between the atomic cores and the valence electron density[52]. The exchange-correlation potential was described using the Perdew-Burke-Ernzerhof (PBE) functional within the generalized gradient approximation (GGA)[53]. A kinetic energy cutoff of 500 eV was chosen to ensure complete convergence. The Brillouin zone was sampled with the k-grid of 3×3×1. The conjugate gradient (CG) method was used for structural relaxation, simultaneously minimizing total energy and interatomic forces. The convergence tolerance for the total energy was set at 10^{-5} eV, and the residual force on each atom was limited to less than 0.02 eV/Å. Additionally, dispersion-corrected DFT-D3 schemes were employed to account for van der Waals interactions[54]. The binding energy (ΔE) is calculated using the formula:

$$\Delta E = E_{total} - E_m - E_{ad},$$

E_{total} is the total energy of the system after the adsorbate is attached to the substrate (the binding system). E_m is the energy of the clean substrate or electrode material by itself. E_{ad} is the energy of the free, isolated adsorbate molecule or atom.

The minimum energy pathways and transition states for the reactions were determined using the climbing image nudged elastic band (CI-NEB) method[55].

FDTD and COMSOL simulations

Optical simulations were performed using the finite-difference time-domain (FDTD) method implemented in Ansys Lumerical FDTD 2025. The simulated multilayer stacks were constructed according to the experimental device geometry. To ensure the accuracy of the simulation results, the thickness of each functional layer is uniformly fixed. The reference device was defined as $MAPbI_3$ (200 nm)/Ag (100 nm), and the polymer-modified devices were defined as $MAPbI_3$ (200 nm)/polymer (100 nm)/Ag (100 nm), where the polymer layer was PVA, PS, PVP, PMMA or PBMA. A broadband plane-wave source was incident from the air side over a wavelength range of 300–800 nm with a spectral interval of 1 nm. The wavelength-dependent refractive indices and extinction coefficients of $MAPbI_3$ and the polymers were taken from reported optical constants, and those of Ag were taken from Johnson and Christy. Field monitors were placed near the $MAPbI_3$/polymer/Ag region to extract the interface-local normalized electric-field intensity, $|E|^2$. For polymer-dependent comparison, the averaged $|E|^2$ response of the five polymer-modified devices was subtracted from each individual polymer case to generate the mean-subtracted interfacial field maps. The analysis focused on local electric-field redistribution after optical excitation rather than wavelength-dependent absorption or optical-loss spectra. Finite-element simulations were performed using COMSOL Multiphysics to resolve the electrostatic-field and carrier-density distributions near the $MAPbI_3$/polymer interface. The device was simplified as a one-dimensional multilayer stack along the thickness direction. P3HT and $MAPbI_3$ were treated as semiconductor regions governed by Poisson and drift-diffusion equations, whereas the polymer overlayer was treated as a dielectric barrier and interfacial boundary layer. The optical generation profile $G(x)$obtained from the FDTD multilayer optical model was imported as a fixed photogeneration source. The simulations were used to compare polymer-dependent electrostatic and electron-density redistribution at the $MAPbI_3$/polymer interface[56, 57, 58, 59, 60].

Declarations

Data Availability

The authors declare that the experimental data supporting the results of this study can be found in the paper and its Supplementary Information file. The detailed data for the study is available from the corresponding author upon request. Source data are provided in this paper.

Code availability

The custom code used in this study is available from the corresponding authors upon request.

Author Contributions Statement

L.P., D.Z. and J.Y. conceived the project and designed the research. L.P. and S.S. fabricated the devices and performed the optoelectronic and photoelectrical measurements. X.Z. carried out the density functional theory and finite-difference time-domain simulations. L.G. and Y.P. contributed to materials

characterization, data analysis and mechanism interpretation. J.T., Z.R.T., Z.N.T., H.L., H.G., Q.L. and T.L. assisted with device characterization, imaging experiments and data processing. L.P., D.Z. and J.Y. wrote the manuscript with input from all authors. D.Z. and J.Y. supervised the project. All authors discussed the results and commented on the manuscript.

Competing Interests Statement

The authors declare no competing interests.

Acknowledgements

This work was financially supported by the General Program (62275041) and Youth Program (52502166) of the National Science Foundation of China. Supported by the Sichuan Province Major Science and Technology Projects (Grant Nos. 2025ZDZX0088 and 2024ZDZX0030).

References

1. Han X et al (2024) Ultraweak light-modulated heterostructure with bidirectional photoresponse for static and dynamic image perception. Nat Commun 15:10430
2. Wang M, Cao F, Meng L, Wang M, Li L (2025) Direct integration of optoelectronic arrays with arbitrary non-developable structures. Nat Mater 24:1778–1784
3. Yang C et al (2026) Three-terminal reconfigurable volatile/nonvolatile light-emitting memristor for integrated neuromorphic display systems. Adv Mater, e73239
4. Li N et al (2022) Gate-tunable large-scale flexible monolayer MoS2 devices for photodetectors and optoelectronic synapses. Nano Res 15:5418–5424
5. Mennel L et al (2020) Ultrafast machine vision with 2D material neural network image sensors. Nature 579:62–66
6. Wang T-Y et al (2021) Reconfigurable optoelectronic memristor for in-sensor computing applications. Nano Energy 89:106291
7. Zhang Z et al (2022) All-in-one two-dimensional retinomorphic hardware device for motion detection and recognition. Nat Nanotechnol 17:27–32
8. Abbas Z et al (2025) Chalcogenide-based brain-inspired photo-synapses for neuromorphic vision sensor: An experimental and theoretical study. Small 21:e04294
9. Gao S et al (2019) An oxide Schottky junction artificial optoelectronic synapse. ACS Nano 13:2634–2642
10. Zhou Z et al (2025) Low energy consumption photoelectric memristors with multi-level linear conductance modulation in artificial visual systems application. Nano-Micro Lett 17:317

11. Hao Z et al (2022) Retina-inspired self-powered artificial optoelectronic synapses with selective detection in organic asymmetric heterojunctions. Adv Sci 9:2103494
12. Miao X et al (2024) Robust self-powered optoelectronic synapses based on epitaxial InSe/GaN heterojunction with interfacial charge-trapping layer. Adv Opt Mater 12:2400358
13. Zhao P et al (2023) Self-powered optoelectronic artificial synapses based on a lead-free perovskite film for artificial visual perception systems. J Mater Chem C 11:6212–6219
14. Dang B et al (2024) Reconfigurable in-sensor processing based on a multi-phototransistor-one-memristor array. Nat Electron 7:991–1003
15. Bousoulas P et al (2026) Low-power perovskite-based memristors enable fused reservoir computing and neuromorphic vision with highly accurate color perception. Small 22:e08167
16. John RA et al (2018) Synergistic gating of electro-iono-photoactive 2D chalcogenide neuristors: coexistence of hebbian and homeostatic synaptic metaplasticity. Adv Mater 30:1800220
17. Ferrarese Lupi F et al (2024) Synaptic plasticity and visual memory in a neuromorphic 2D memitter based on WS_2 monolayers. Adv Funct Mater 34:2403158
18. Cui D et al (2025) Versatile optoelectronic memristor based on wide-bandgap Ga2O3 for artificial synapses and neuromorphic computing. Light: Sci Appl 14:161
19. Tan H, van Dijken S (2023) Dynamic machine vision with retinomorphic photomemristor-reservoir computing. Nat Commun 14:2169
20. Jiang J et al (2024) Retina-like chlorophyll heterojunction-based optoelectronic memristor with all-optically modulated synaptic plasticity enabling neuromorphic edge detection. Adv Funct Mater 34:2409677
21. Zhou J et al (2025) Optoelectronic polymer memristors with dynamic control for power-efficient in-sensor edge computing. Light: Sci Appl 14:309
22. Li QX et al (2026) Feedback neurons based on perovskite memristor with nickel single-atom engineered reduced graphene oxide cathode. Nat Commun 17:3085
23. Liu T et al (2025) Chelated tin halide perovskite for near-infrared neuromorphic imaging array enabling object recognition and motion perception. Nat Commun 16:4261
24. Liu X et al (2026) Artificial refractory neuron based on $Cs_2AgBiBr_6$ nano ionic memristor for efficient motion information processing. Adv Mater, e19352
25. Du P et al (2026) Bio-inspired halide perovskite photodetectors and memristors. Adv Funct Mater 36:e32096
26. John RA et al (2018) Ionotronic halide perovskite drift-diffusive synapses for low-power neuromorphic computation. Adv Mater 30:e1805454
27. Sun Y et al (2019) Photoelectric synaptic plasticity realized by 2D perovskite. Adv Funct Mater 29:1902538
28. Zhang X et al (2026) Self-powered photo triggered memristor array with pW-level computing for monolithic in-sensor vision. Adv Mater 38:e23017

29. Wang Y et al (2024) Monolithic 2D perovskites enabled artificial photonic synapses for neuromorphic vision sensors. Adv Mater 36:2311524
30. Zhang F et al (2024) Photoinduced nonvolatile memory transistor based on lead-free perovskite incorporating fused π-conjugated organic ligands. Adv Mater 36:2307326
31. He Z et al (2025) Perovskite retinomorphic image sensor for embodied intelligent vision. Sci Adv 11:eads2834
32. Gong J et al (2021) Methylammonium halide-doped perovskite artificial synapse for light-assisted environmental perception and learning. Mater Today Phys 21:100540
33. Xie Z et al (2024) Unraveling dual operational mechanisms in an air-stable all inorganic perovskite for nonvolatile memory and neuromorphic computing. ACS Energy Lett 9:948–958
34. Kim D et al (2023) Enhanced photostability of hollow mixed halide wide-bandgap perovskite films. ACS Energy Lett 8:5221–5228
35. Du Q et al (2025) Collaborative passivation of defects and enhancing crystallization enabled by an additive with multiple active sites for inverted perovskite solar cells. Chem Eng J 521:166733
36. Yang X et al (2021) Buried interfaces in halide perovskite photovoltaics. Adv Mater 33:e2006435
37. Li J et al (2025) Homogenizing the halogen distribution via a multifunctional fluorine-containing additive toward high-performance inverted wide-bandgap perovskite solar cells. Adv Funct Mater 35
38. Tang Z et al (2016) Investigating relation of photovoltaic factors with properties of perovskite films based on various solvents. Nano Energy 21:51–61
39. Xu D et al (2022) Constructing molecular bridge for high-efficiency and stable perovskite solar cells based on P3HT. Nat Commun 13:7020
40. Wang X, Liu S, Wang H, Luo J (2024) Side chain functional molecule additives for efficient and stable perovskite solar cells. Adv Funct Mater 34:2403104
41. Zhang M et al (2019) Reconfiguration of interfacial energy band structure for high-performance inverted structure perovskite solar cells. Nat Commun 10:4593
42. Tian J et al (2026) Modifying 6,6-Phenyl-C61-butyric acid methyl ester with a multifunctional organic molecule improves performance of electron transport layer and passivates defects in inverted perovskite solar cell. Solar RRL 10:e70310
43. Yang T et al (2026) Stereoelectronic manipulation of ligands for perovskite solar cells. Nature
44. De Keersmaecker M et al (2025) Activated corrosion and recovery in lead mixed-halide perovskites revealed by dynamic near-ambient pressure X-ray photoelectron spectroscopy. J Am Chem Soc 147:8881–8892
45. Liu C et al (2018) Mechanofluorochromic carbon nanodots: controllable pressure-triggered blue- and red-shifted photoluminescence. Angew Chem Int Ed Engl 57:1893–1897
46. Yang L, Bashir R (2008) Electrical/electrochemical impedance for rapid detection of foodborne pathogenic bacteria. Biotechnol Adv 26:135–150

47. Pingree LSC, Russell MT, Marks TJ, Hersam MC (2006) Field dependent negative capacitance in small-molecule organic light-emitting diodes. J Appl Phys 100:044502
48. Yan C et al (2022) Unraveling hole interlayer-dependent interfacial energetics of LEDs. Nano Energy 102:107621
49. Pan L et al (2024) Bidirectional inhibiting interfacial ion migration in the inorganic hole transport layer for perovskite light-emitting diodes. Small 20:e2405528
50. Cui D et al (2025) Self-powered halide perovskite optoelectronic synaptic memristors for reconfigurable logic and reservoir computing applications. Nano Lett 25:15705–15713
51. Kresse G, Hafner J (1993) Ab initio molecular dynamics for liquid metals. Phys Rev B 47:558
52. Kresse G, Joubert D (1999) From ultrasoft pseudopotentials to the projector augmented-wave method. Phys Rev B 59:1758
53. Perdew JP, Burke K, Ernzerhof M (1996) Generalized gradient approximation made simple. Phys Rev Lett 77:3865
54. Grimme S, Antony J, Ehrlich S, Krieg H (2010) A consistent and accurate ab initio parametrization of density functional dispersion correction (DFT-D) for the 94 elements H-Pu. J Chem Phys 132:154104
55. Henkelman G, Uberuaga BP, Jónsson H (2000) A climbing image nudged elastic band method for finding saddle points and minimum energy paths. J Chem Phys 113:9901–9904
56. Hong PT, Nguyen HQ, Nghiem HTM (2023) Complex refractive index measurements of poly (methyl methacrylate)(PMMA) over the UV-VIS-NIR region. Opt Continuum 2:2280–2289
57. Phillips LJ et al (2015) Dispersion relation data for methylammonium lead triiodide perovskite deposited on a (100) silicon wafer using a two-step vapour-phase reaction process. Data brief 5:926–928
58. Schnepf MJ et al (2017) Nanorattles with tailored electric field enhancement. Nanoscale 9:9376–9385
59. Vani G, Sudha N (2013) Optical properties of PVP based polymer electrolyte films. Int J Res Eng Adv Technol 3:7–12
60. Zhang X, Qiu J, Li X, Zhao J, Liu L (2020) Complex refractive indices measurements of polymers in visible and near-infrared bands. Appl Opt 59:2337–2344

Figures

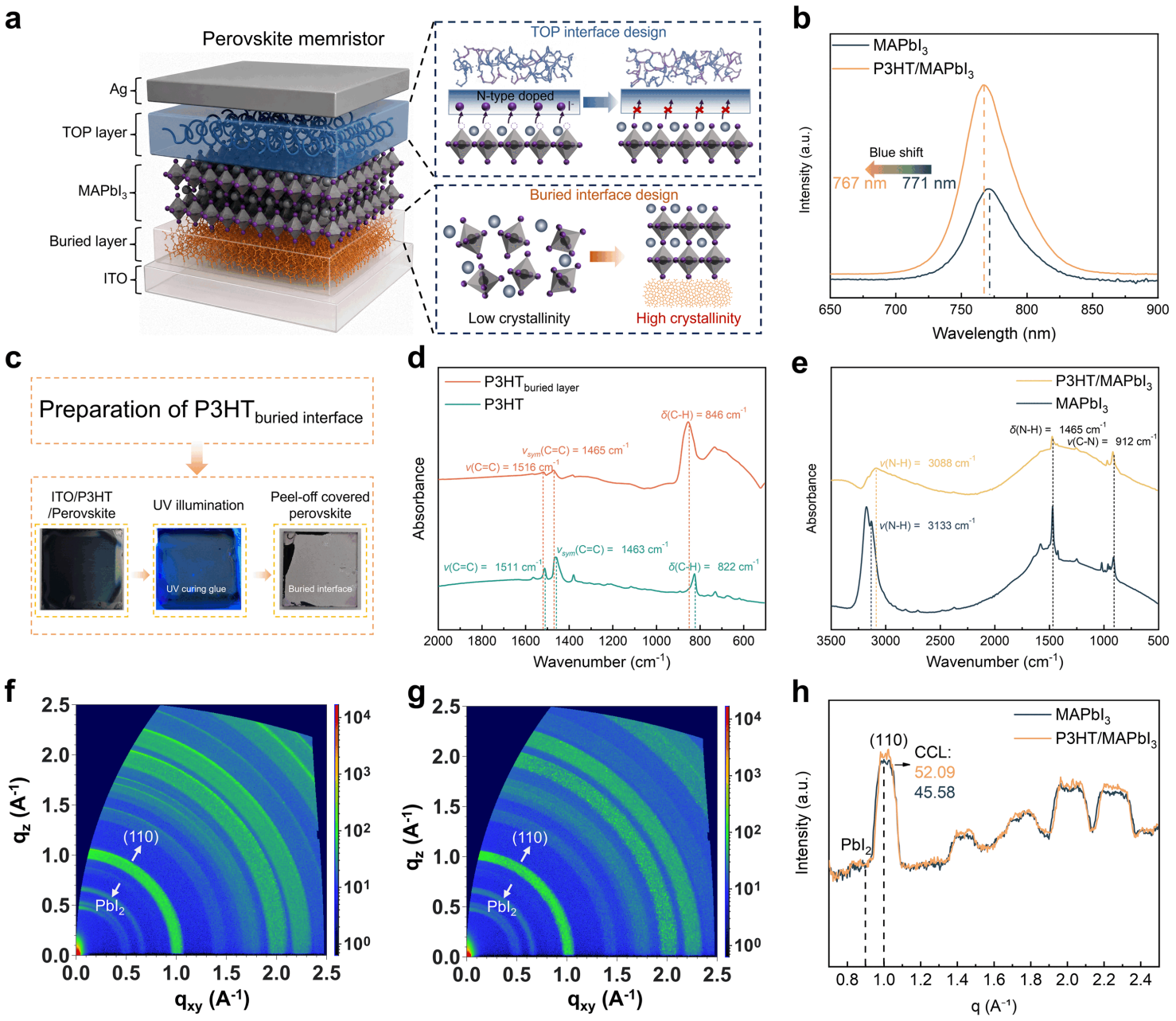


Figure 1

Crystallization-directed buried interface. a) Vertically partitioned interfacial architecture of self-powered perovskite photomemristors. b) Photoluminescence (PL) spectra of $MAPbI_3$ films deposited on the substrate without P3HT and on the P3HT buried interface. c) Schematic illustration of the peel-off process used to remove the $MAPbI_3$ overlayer and expose the P3HT buried interface. d) Fourier-transform infrared spectroscopy (FTIR) spectra of the pristine P3HT film and the buried-interface P3HT layer after peel-off. e) FTIR spectra of $MAPbI_3$ films on substrates without P3HT and on the P3HT buried interface. Two-dimensional grazing-incidence wide-angle X-ray scattering (GIWAXS) images of $MAPbI_3$ films on the f) substrate without P3HT and g) P3HT buried interface. h) Azimuthally integrated GIWAXS intensity profiles from f) and g).

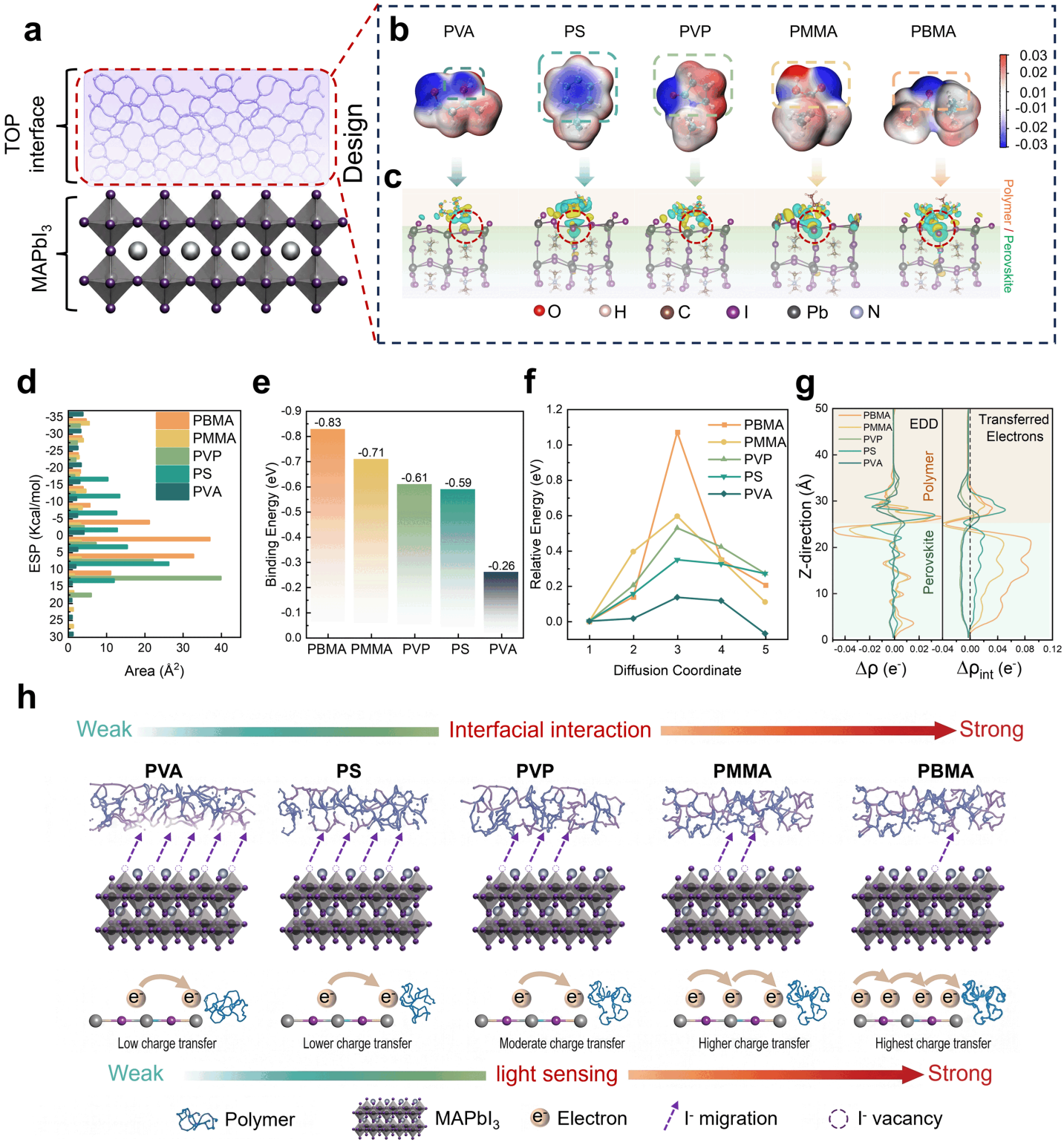


Figure 2

Side-chain-defined top recovery interphase for ion-electron regulation. a) Schematic illustration of top-interface molecular engineering at the $MAPbI_3$/polymer interface. b) Electrostatic-potential maps of the side groups of PVA, PS, PVP, PMMA and PBMA, with the selected regions highlighted for subsequent analysis. c) Differential charge-density maps of the polymer/$MAPbI_3$ adsorption configurations. d) Statistical comparison of the electrostatic-potential values extracted from the highlighted side-group

regions in b). e) Calculated binding energy of the polymer/$MAPbI_3$ interfaces. f) Calculated I^- migration-energy barriers in $MAPbI_3$ after polymer adsorption. g) Electron-density-difference maps and transferred-electron profiles of the polymer/$MAPbI_3$ interfaces. h) Schematic illustration of the polymer-dependent interfacial interaction at the $MAPbI_3$ top surface.

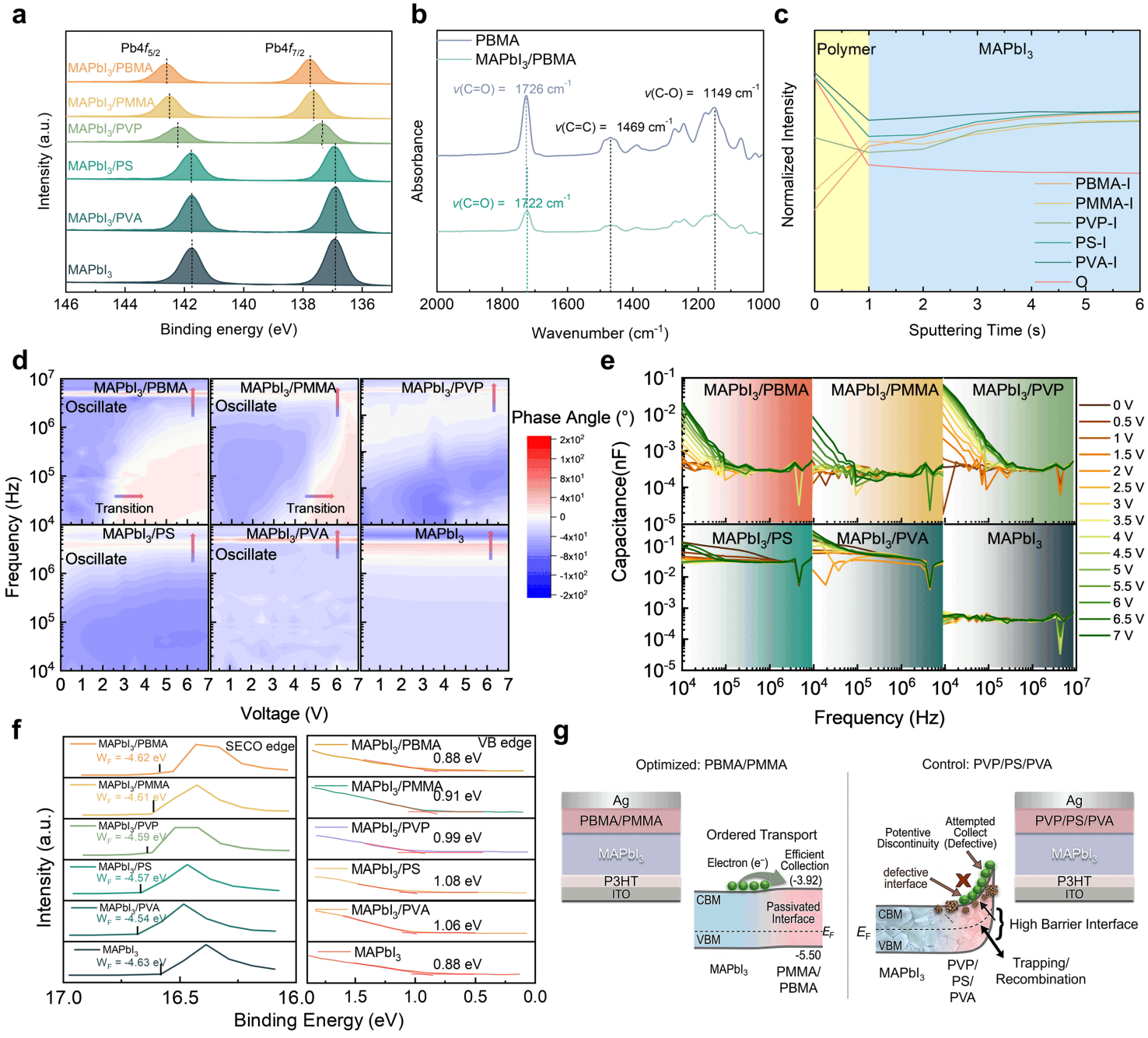


Figure 3

Top-interface ion-electron coupling mechanism. a) X-ray photoelectron spectroscopy (XPS) spectra of Pb in $MAPbI_3$ films with different polymer top interfaces. b) FTIR spectra of pristine PBMA and PBMA deposited on $MAPbI_3$. c) Depth profiles of I- and O-containing fragments in P3HT/$MAPbI_3$/polymer heterostructures. The turning point of the O signal represents the $MAPbI_3$/polymer interface. d) Voltage-

dependent impedance magnitude of the ITO/P3HT/$MAPbI_3$/polymer/Ag devices, reflecting polymer-regulated resistive transport and interfacial relaxation. e) Capacitance-voltage characteristics of the complete devices, revealing polymer-dependent interfacial charge accumulation and polarization behavior. f) Ultraviolet photoelectron spectroscopy (UPS) spectra of the perovskite/polymer interfaces at an etching time of 30 s. g) Schematic illustration of the interfacial ion-electron coupling processes in the P3HT/$MAPbI_3$/polymer heterostructure.

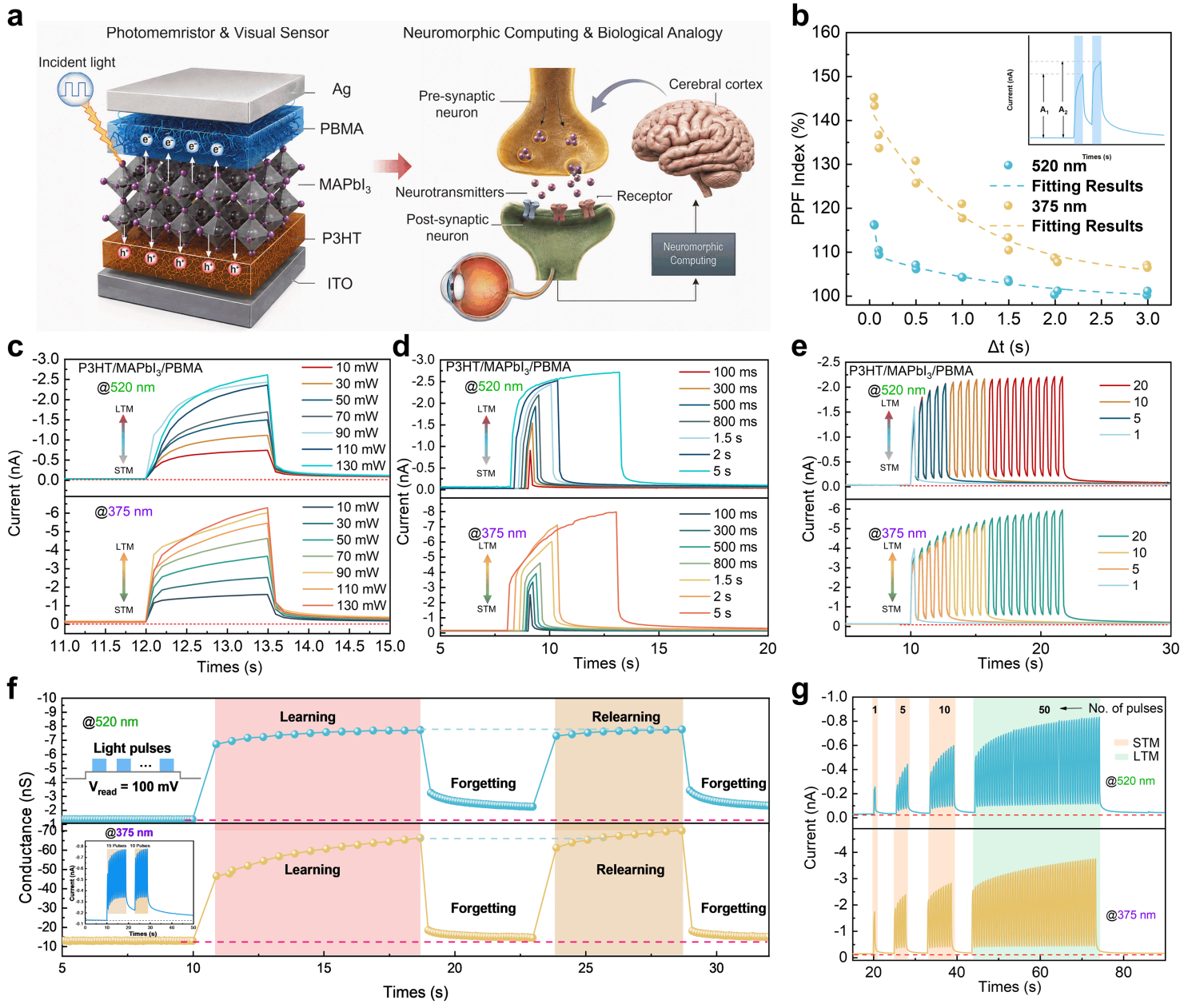


Figure 4

Self-powered photomemristors. a) Schematic illustration of the ITO/P3HT/$MAPbI_3$/PBMA/Ag photomemristor and its analogy to the human visual pathway, where optical perception, retinal synaptic transmission and visual recognition are represented by light sensing, self-powered postsynaptic current and history-dependent conductance memory, respectively. b) Paired-pulse facilitation index of the

optimized ITO/P3HT/$MAPbI_3$/PBMA/Ag device under 520 and 375 nm optical excitation as a function of interpulse interval. c) Single-pulse synaptic responses under different optical power densities at 520 and 375 nm (pulse duration, 1.5 s). d) Single-pulse synaptic responses under different pulse durations at 520 and 375 nm. e) Synaptic responses under different optical pulse numbers at 520 and 375 nm (pulse duration, 300 ms). f) Conductance modulation during learning, forgetting and relearning under sequential optical pulse trains at 520 and 375 nm. g) Synaptic responses under 1, 5, 10 and 50 optical pulses at 520 and 375 nm (pulse duration, 300 ms), showing the transition from short-term memory to long-term memory.

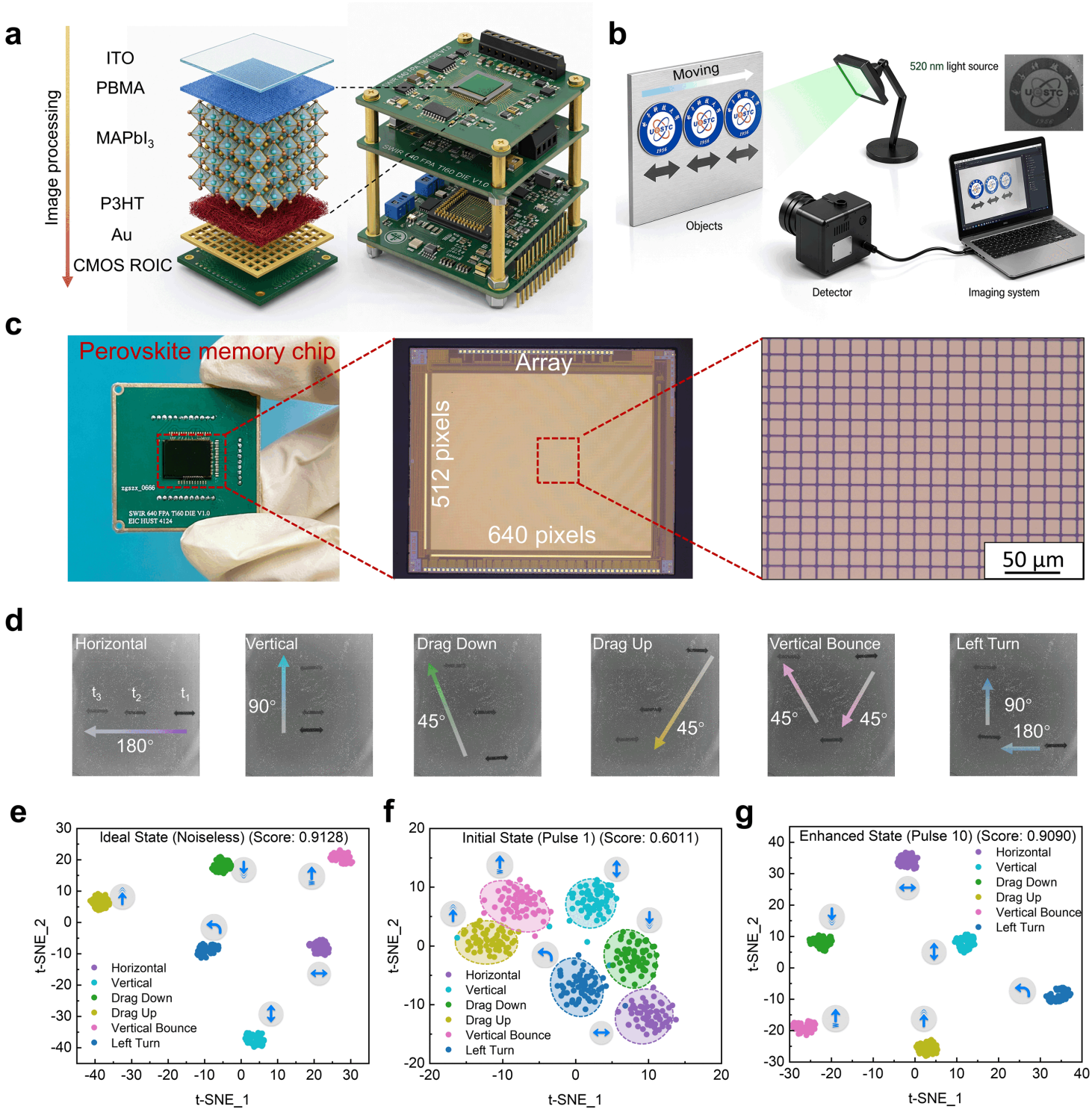


Figure 5

CMOS-integrated hardware-level motion-state recognition and algorithmic trajectory clustering. a) Schematic illustration of the CMOS-integrated visual platform, showing the optical window, perovskite photomemristor array and readout integrated circuit (ROIC) module. b) Schematic illustration of the imaging platform, in which the perovskite/ROIC module is integrated into the camera unit for optical-pattern acquisition and memory-assisted readout. c) Array layout of the perovskite visual chip, showing a 640 × 512-pixel array with a pixel size of 15 μm. d) Hardware-level time-resolved imaging of six motion states recorded at t_1 = 0 s, t_2 = 1.5 s and t_3 = 3 s, showing trajectory retention encoded by the perovskite photomemristor array. e-g) Algorithmic clustering evaluation of six-direction motion features using device-recorded trajectory maps obtained from e) the ideal noiseless state, f) the initial pulse-1 state and g) the enhanced pulse-10 state, with clustering scores of 0.9128, 0.6011 and 0.9090, respectively.

Supplementary Files

This is a list of supplementary files associated with this preprint. Click to download.

- SupportingInformation.docx